Bioelectrochemistry 145 (2022) 108094

Contents lists available at ScienceDirect

Bioelectrochemistry

journal homepage: www.journals.elsevier.com/bioelectrochemistry

A novel pomegranate-inspired bifunctional electrode materials design for acetylcholinesterase biosensor and methanol oxidation reaction

Wenbo Wei [a,1], Huangcong Tang [a,1], Sheying Dong [a,*], yile Fu [a], Tinglin Huang [b]

[a] School of Chemistry and Chemical Engineering, Xi'an University of Architecture and Technology, Xi'an 710055, China
[b] School of Environmental and Municipal Engineering, Xi'an University of Architecture and Technology, Xi'an 710055, China

ARTICLE INFO

Keywords:
Pomegranate-like architecture
Bifunctional electrocatalysts
Methanol oxidation reactions
Biosensors

ABSTRACT

A pomegranate-inspired bifunctional electrode material based on Ni/NiO nanoparticle embedded in nitrogen-doped, partially graphitized carbon framework (Ni/NiO@NPGC) was designed and prepared for the construction of novel electrochemical biosensor and methanol oxidation reaction (MOR). Profiting from its special structure and function, Ni/NiO@NPGC was employed as a matrix immobilizing acetylcholinesterase (AChE) for methyl parathion (MP) sensor. The developed biosensor was proved to have wide linear range (1.0×10^{-14}-1.0×10^{-8} g mL^{-1}), low detection limit (3.5×10^{-15} g mL^{-1}), and good stability for the determination of MP in practical samples. In addition, the Ni/NiO@NPGC electrode exhibited high electrocatalytic activity (specific activity 73.1 mA cm^{-2}) and durability for the MOR in alkaline medium. The results were mainly attributed to the pomegranate-like architecture structure with pyridinic N and carbon frame of Ni/NiO@NPGC, which ensured the electrochemical activities of all nanoparticles and immobilization of enzyme. In addition, the metal oxide was well dispersed to prevent from self-agglomeration and kept mass transfer paths. The work provides a reference for the development of high-performance bifunctional electrode material for the biosensor and MOR.

1. Introduction

Electrochemical biosensors have been attractive for decades because of their high sensitivity, on-site analysis, quick response, and relatively cheaper instrumentation [1–3]. However, these biosensors could suffer from lower loading capacity and more leakage of enzymes molecules [4]. Therefore, it is effortful to search electrode materials with better biocompatibility and higher electrochemical activity for enzyme immobilization to improve the sensitivity and stability of biosensors. In addition, direct methanol fuel cells (DMFCs) are universally concerned as promising renewable energy [5,6]. As the MOR is the critical process for DMFCs, it is essential to design and synthesize efficient electrocatalyst for MOR [7]. Currently, precious metal-based electrode materials such as Pt, Pd, and Au as well as alloys have been industriously studied, which showed good electrocatalytic properties [8,9]. However, the high costs of those catalysts slowed down their widespread application [10]. Consequently, a considerable number of researches focus on non-noble electrocatalysts for MOR.

Non-precious transition metals (Co, Ni, Fe et al.) and relative materials have gained extended attention working as electrode materials, which attributed to low cost, wide potential window, high electronic conductivity and electrocatalytic activity towards a considerable amount of redox species and biosensors [11–13]. Among these materials, Ni and NiO are relatively important subjects for electrocatalytic oxidation and biosensing. For example, Tyagi et al. designed a bioelectrode based on NiO nanorods for the development of an efficient urea biosensor [13]. Nevertheless, these proposed materials have experienced counterproductive catalytic activity due to self-aggregation and constitutionally poor electrical conductivity.

Generally, for the immobilization of enzymes and the catalytic reaction, the performance of electrode materials is determined by the surface structure and chemical composition [14]. To address this importance, nanomaterials with multiple morphologies have been designed to produce more catalytic active sites and improve diffusion of reactive species [15,16]. In addition, conductive carbon materials have also been brought into catalysts to improve the conductivity and structural stability of catalysts [17,18]. For instance, the Co_3O_4 nanocrystal/rGO exhibited excellent catalytic activity derived from synergetic chemical coupling effects [18]. Recent research has shown that metal-based core–shell nanoparticles (NPs) and nitrogen-doping can

* Corresponding author.
E-mail address: dongsyy@126.com (S. Dong).
[1] These authors contributed equally to this work.

https://doi.org/10.1016/j.bioelechem.2022.108094
Received 22 December 2021; Received in revised form 1 March 2022; Accepted 8 March 2022
Available online 11 March 2022

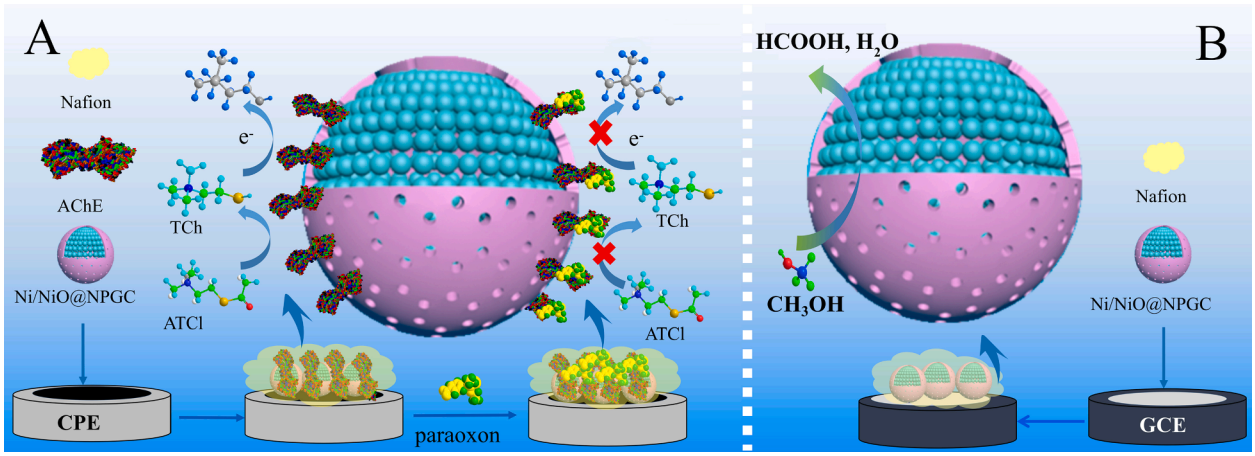

Fig. 1. Schematic of the procedure for NF/AChE/NF-Ni/NiO@NPGC/CPE (A) and NF-Ni/NiO@NPGC/GCE.

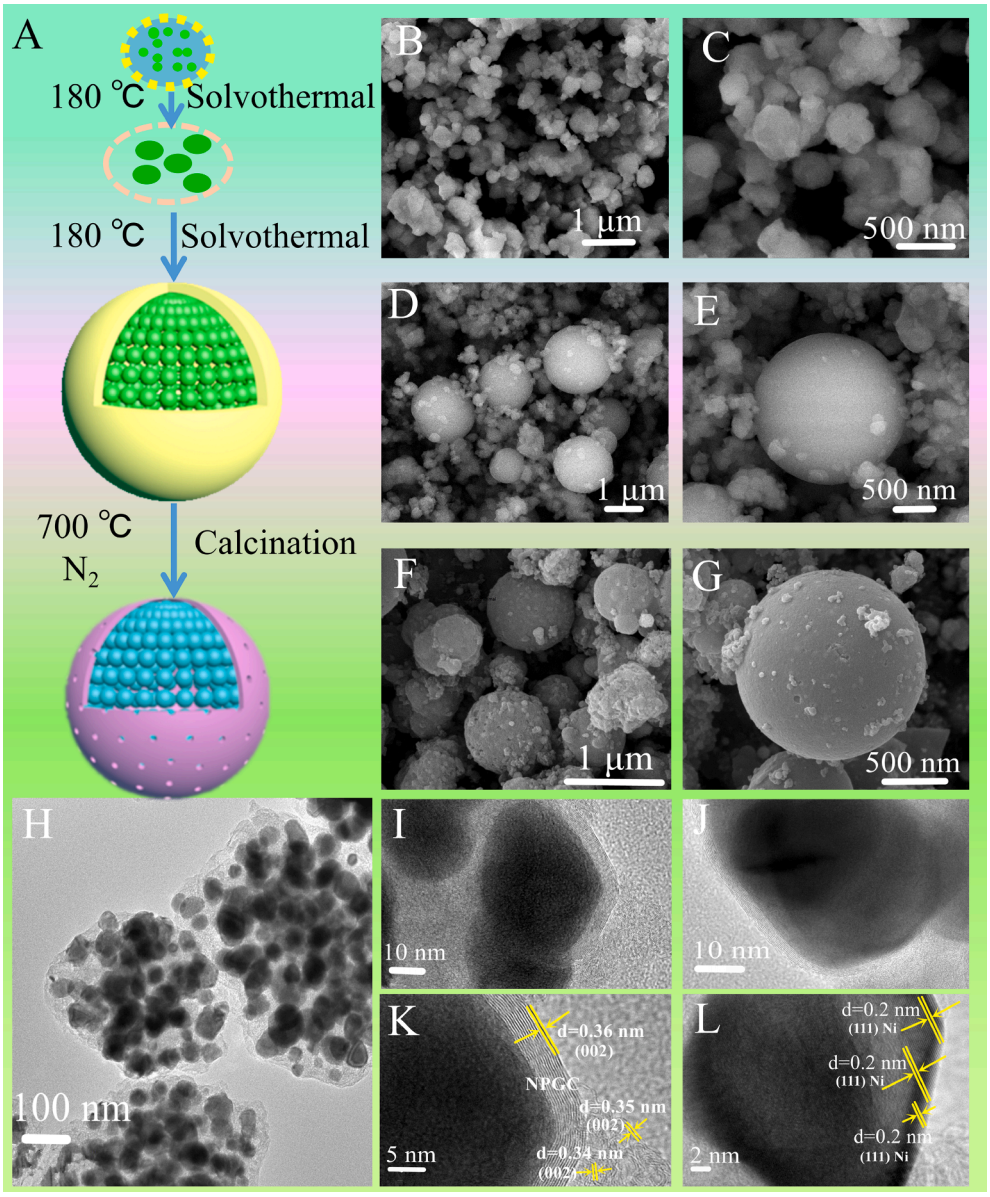

Fig. 2. (A) Schematic of the procedure for Ni/NiO@NPGC ; (B-G) SEM images of $Ni(OH)_2$-glycerate (B and C), $Ni(OH)_2$-glycerate@CN (D and E), Ni/NiO@NPGC (F and G); (H) the TEM of Ni/NiO@NPGC; (I-L) the HRTEM of Ni/NiO@NPGC.

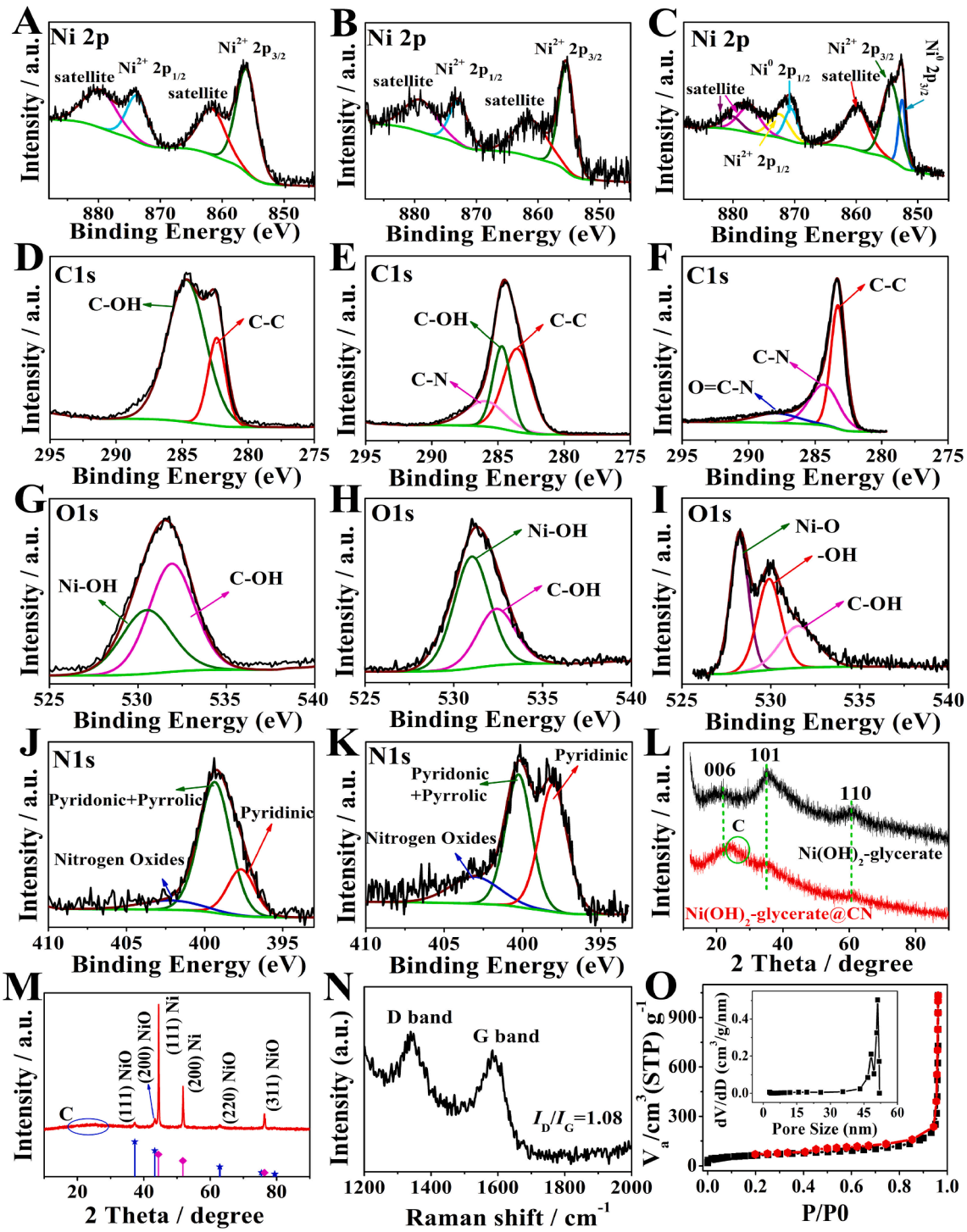

Fig. 3. (A-K) XPS results of the $Ni(OH)_2$-glycerate, $Ni(OH)_2$-glycerate@CN and Ni/NiO@NPGC samples: (A-C) Ni 2p spectra, (D-F) C1s spectra, (G-I) O1s spectra, the left, middle and right columns are the results from the Control, PCNS-4 and PCNS samples, respectively, (J-K) N1s spectra of $Ni(OH)_2$-glycerate@CN (J) and Ni/NiO@NPGC (K); (L and M) X-ray diffraction pattern of the $Ni(OH)_2$-glycerate, $Ni(OH)_2$-glycerate@CN and Ni/NiO@NPGC samples; (N) Raman spectra of the Ni/NiO@NPGC; (O) Nitrogen adsorption–desorption isotherm and pore size distribution of Ni/NiO@NPGC.

remarkably accelerate the electron transfer in the electrocatalytic reaction [19]. Although there are many studies on the subject, reasonable design strategy and efficient improvement of needed high-performance electrode materials for the immobilization of enzyme and catalytic reaction are yet limited.

Herein, a novel pomegranate-inspired nanomaterial with nitrogen-doped and graphitized carbon framework (Ni/NiO@NPGC) was designed, prepared and characterized. Moreover, the Ni/NiO@NPGC was utilized as an immobilization matrix for AChE biosensor. Meantime, methanol was selected as a target molecule to investigate the electrocatalytic activities of the material in the alkaline solution.

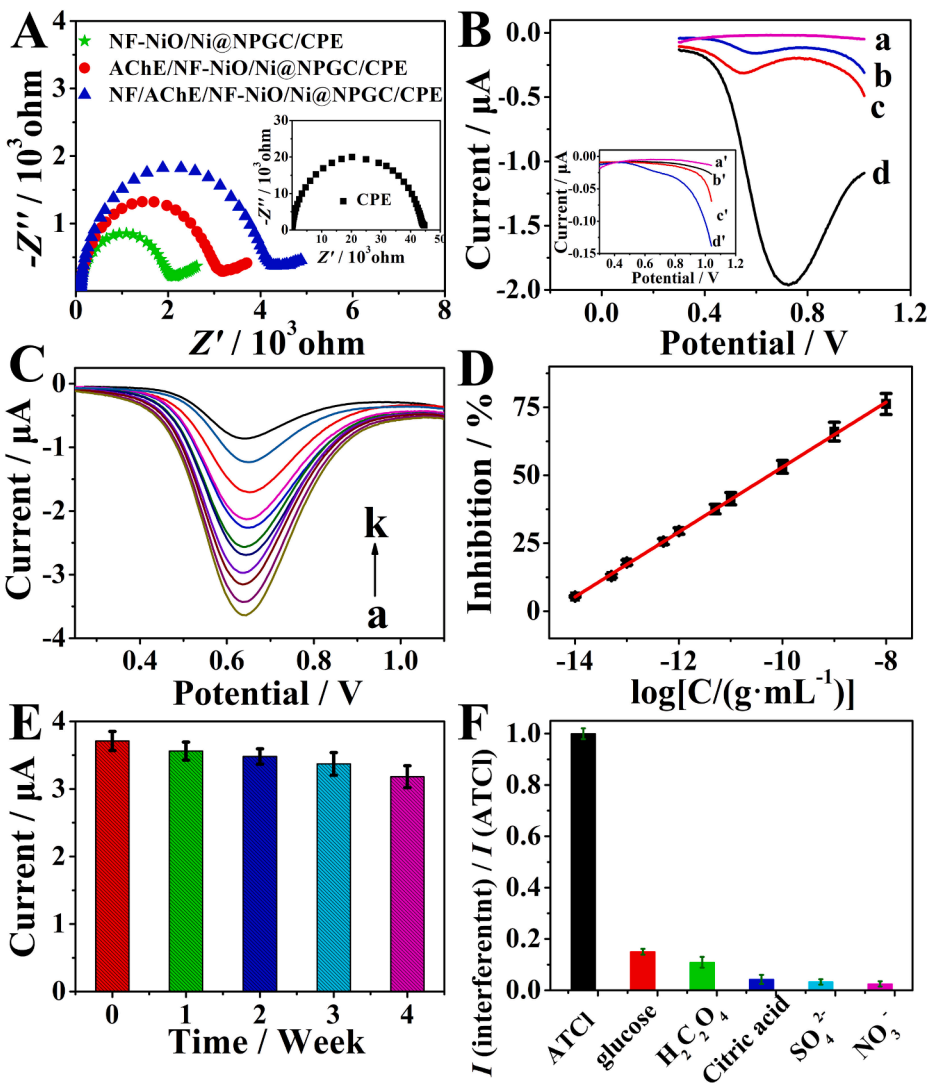

Fig. 4. (A) EIS of CPE, NF-Ni/NiO@NPGC/CPE, AChE/NF-Ni/NiO@NPGC/CPE and NF/AChE/NF-Ni/NiO@NPGC/CPE in the solution of 5.0 mM $K_3Fe(CN)_6/K_4Fe(CN)_6$ (1:1) containing 0.1 M KCl. (B) DPVs of NF/AChE/CPE (a/a′), NF/AChE/NF/CPE (b/b′), NF-Ni/NiO@NPGC/CPE (c/c′) and NF/AChE/NF-Ni/ NiO@NPGC/CPE (d/d′) within /without 1.5 mM ATCI in 0.1 M pH 7.5 PBS. (C) DPV response of NF/AChE/NF-Ni/NiO@NPGC /CPE in 0.1 M pH 7.5 PBS containing 1.5 mM ATCl after incubation with paraoxon for 10 min. Methyl parathion concentration (a-j): 0, 10^{-14}, 5×10^{-14}, 10^{-13}, 5×10^{-13},10^{-12}, 10^{-11}, 10^{-10}, 10^{-9} and 10^{-8} g·mL^{-1}. (D) Inhibition curve of NF/AChE/NF-Ni/NiO@NPGC/CPE biosensor for methyl parathion determination by DPV. (E) Shelf-life of NF/AChE/NF-NiO/Ni@NPGC /CPE after 4 weeks. (F) The ratio of the signal of NF/AChE/NF-NiO/Ni@NPGC/CPE for interference to that for ATCl. The response currents were obtained at the biosensor on successive injection of 0.5 mM ATCl, 0.5 mM glucose, 0.5 mM $H_2C_2O_4$, 0.5 mM citric acid, 0.5 mM SO_4^{2-}, 0.5 mM NO_3^- in pH 7.5 PBS at 0.63 V.

Table 1
Comparisons of the proposed biosensors to detect methyl parathion with other biosensors reported.

Biosensors	Linear range	Detection limit	References
AChE-LDH/GCE	0.005–0.3 × $10^{-6}$and 0.3–4.0 × 10^{-6} g·mL^{-1}	0.6 × 10^{-9} g·mL^{-1}	[33]
AChE/AuNPs-CSs /BOD	2.6 × 10^{-12}- 2.6 × 10^{-6} g·mL^{-1}	1.3 × 10^{-13} g·mL^{-1}	[34]
NF/AChE / NF-$NiCo_2S_4$/ CPE	10^{-12}-10^{-8} g·mL^{-1}	4.2 × 10^{-13} g·mL^{-1}	[35]
NF/AChE/NF-Ni/ NiO@NPGC/CPE	10^{-14}-10^{-8} g·mL^{-1}	3.5 × 10^{-15} g·mL^{-1}	This work

2. Material and methods

2.1. Synthesis of Pomegranate-Like Nanocomposites.

$Ni(NO_3)_2{\cdot}6H_2O$ (0.112 g) and glycerol (8.0 mL) were dissolved in isopropanol (40 mL), then transferred to autoclave (50 mL) and kept at 180 °C for 6 h. The obtained light green powder ($Ni(OH)_2$-glycerate) was dried under vacuum at 80 °C.

For the synthesis of Ni/NiO@NPGC nanocomposites, $Ni(OH)_2$-glycerate powder was well dispersed in isopropanol (40 mL), and then added glucose solution (1.0 M, 4.0 mL), urea (0.480 g), and glycerol (8 mL) and homogeneous dispersion. The mixture was transferred to a 50 mL autoclave and kept at 180 °C for 4 h. The precipitate ($Ni(OH)_2$-glycerate@CN) was separated by centrifugation and washing, respectively. The fine dark brown powder obtained after drying under vacuum at 80 °C was annealed under N_2 atmosphere at 700 ℃ (5 °C/min) for 200 min to get the final product.

2.2. Preparation of the modified electrodes.

Fig. 1A illustrates the process by which AChE are immobilized on Ni/NiO@NPGC modified electrode to obtain AChE/ NF-Ni/NiO@NPGC/CPE. A detailed description of the preparation process and the detection of methyl parathion (MP) as well as calculation procedure are shown in the Supporting Information S1 and S2.

The GCE modified electrodes were prepared as follows: A GCE was polished with Al_2O_3, and washed with water. 3 mg Ni/NiO@NPGC catalyst, 800 μL deionized water and 50 μL NF (0.5 wt%) solution was mixed to obtain the catalyst slurry. Then, 10 μL slurry was spread on a freshly polished GCE and dried to obtain NF-Ni/NiO@NPGC/GCE (Fig. 1B). The diameter of the GCE was 3 mm, and the geometric surface area was 0.0706 cm^2.

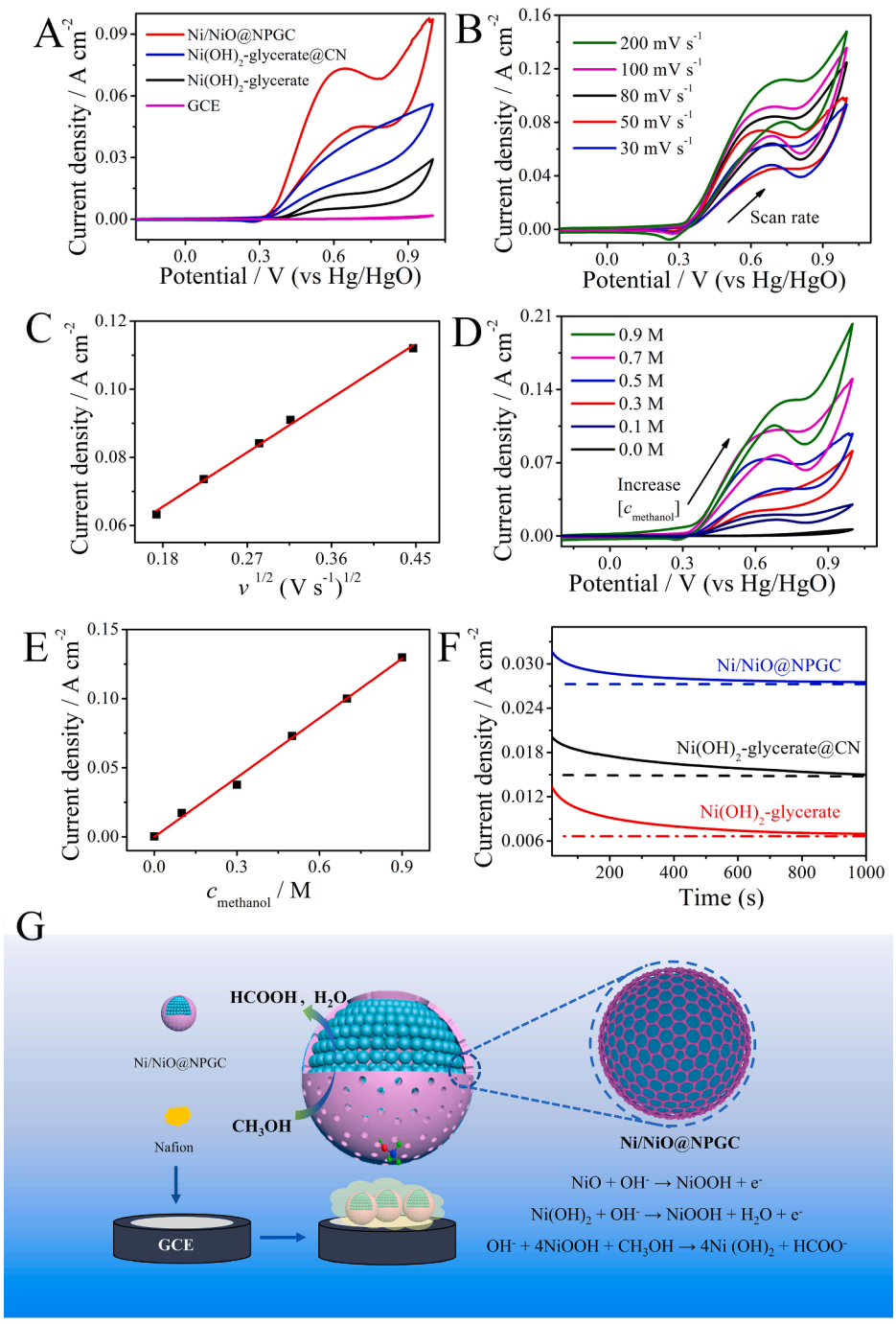

Fig. 5. (A) CVs of $Ni(OH)_2$-glycerate, $Ni(OH)_2$-glycerate@CN and Ni/NiO@NPGC for methanol electrooxidation in 1.0 M KOH solution at a scan rate of 50 mV s^{-1}. (B) CV curves of NF-Ni/NiO@NPGC/GCE at different scan rates. (C) The relationship between peak oxidation current and the square root of scan rate for NF-Ni/NiO@NPGC/GCE. (D) Cyclic voltammograms for Ni/NiO@NPGC in 1.0 M KOH solution in the presence of different concentrations of methanol at a scan rate of 50 mV s^{-1}. (E) Relationship between the oxidation peak current densities and the concentrations of methanol. (F) Chronoamperograms of $Ni(OH)_2$-glycerate, $Ni(OH)_2$-glycerate@CN and Ni/NiO@NPGC in the presence of 0.5 M methanol in 1.0 M KOH solution at a potential step of + 0.65 V for 1000 s. (G) Mechanism of NF-Ni/NiO@NPGC/GCE.

3. Results and discussion

3.1. Composition and structural Characterization.

The preparation process of pomegranate-like nanocomposites is illustrated in Fig. 2A, which involves the directed growth of pomegranate-like Ni nanocomposites inside $Ni(OH)_2$-glycerate@CN, subsequently pyrolyzed to achieve seeds embedded in the carbon layer. From the scanning electron microscopy (SEM) image in Fig. 2B, it is observed that $Ni(OH)_2$-glycerate nanoparticles possesses many particles varied in size. The irregular spherical shape of the $Ni(OH)_2$-glycerate is observed in its SEM images recorded at high magnification (Fig. 2C). Fig. 2D and E display the SEM and magnified SEM images of uniform pomegranate-like $Ni(OH)_2$-glycerate@CN that possesses spherical morphology with smooth surface, which results from $Ni(OH)_2$-glycerate nanoparticles encapsulated by the nitrogen-doped carbon framework. Fig. 2F and G show SEM images of the resulting Ni/NiO@NPGC composite. As shown in high-magnification SEM (Fig. 2G), the porous structure on the Ni/NiO@NPGC ball was successfully obtained by thermal decomposition of $Ni(OH)_2$-glycerate@CN. Furthermore, Fig. 2H displays a transmission electron microscopy (TEM) image of the composites where a pomegranate-like construction was found with seeds embedded in the carbon layer. The high-resolution TEM (HRTEM) images display that the carbon layer is highly graphitized and the Ni/NiO can also be easily identified (Fig. 2I and J). The graphitization takes place in the appearance (Fig. 2K) and within the whole composite spheres (Fig. 2I), forming highly conductive carbon framework. Noteworthily, the carbon layer is still porous, which will benefit to mass

transfer in electrode reactions. The HRTEM image (Fig. 2L) shows a *d*-spacing of 0.207 nm encapsulated seeds, which corresponds to the interplanar distance of (111) planes of Ni [20]. Because the nanoparticles were implanted in the conductive carbon layer, the conductivity of the composite electrode material can be ameliorated obviously.

The XPS survey spectra of Ni/NiO@NPGC and $Ni(OH)_2$-glycerate@CN are formed of several peaks, including the elements of Ni, C, and O. No N peak are observed in the profile of $Ni(OH)_2$-glycerate (Fig.S-1A). The intensity of N peak is small in $Ni(OH)_2$-glycerate@CN (Fig.S-1B), NiO/Ni@NPGC (Fig.S-1C), indicating that the content of doped nitrogen in the above materials is low. A typical energy dispersive spectroscopy (EDS) spectrum of Ni/NiO@NPGC is shown in Fig. S-1D, the compositions calculated from EDS is consistent with the XPS results. In development, the Ni 2p XPS of $Ni(OH)_2$-glycerate in Fig. 3A and Ni $(OH)_2$-glycerate@CN in Fig. 3B show a doublet at 873.9 and 856.1 eV, corresponding to Ni^{2+} $2p_{1/2}$ and Ni^{2+} $2p_{3/2}$, respectively [21]. By comparison, the Ni 2p XPS spectrum of Ni/NiO@NPGC shows two major peaks centered around 872.2 and 855.5 eV (Fig. 3C), which is the characteristic of a NiO phase. In addition, the Ni 2p XPS spectrum of Ni/NiO@NPGC also shows two peaks centered around 870.2 and 852.6 eV, which are the feature of a Ni phase [22], corresponding to Ni^0 $2p_{1/2}$ and Ni^0 $2p_{3/2}$. For $Ni(OH)_2$-glycerate, the C1s (Fig. 3D) can be disassembled into two peaks centered at 285.6 and 282.4 eV, assigned to C-O and C-C bond, respectively [23]. The C 1s spectrum of $Ni(OH)_2$-glycerate@CN (Fig. 3E) can also be deconvoluted into three peaks centered at 285.9, 284.7 and 283.1 eV, assigned to C-N, C-O, and C-C bond, respectively, which indicates the existence of N element. The deconvoluted C1s peak of Ni/NiO@NPGC (Fig. 3F) consists of mainly three individual peaks that are assigned to C-C, C-N (284.9 eV), and O = C-N, respectively, which indicates the existence of O = C-N type of structures [24]. The O 1s spectra of $Ni(OH)_2$-glycerate and $Ni(OH)_2$-glycerate @CN (Fig. 3G and H) can be deconvoluted into two peaks located at 532.2 and 531.2 eV, corresponding to C-O and Ni-OH groups [25]. By comparison, the deconvoluted O 1s peak of Ni/NiO@NPGC (Fig. 3I) consists of mainly three individual peaks that are assigned to C-OH, –OH (529.9 eV), and Ni-O (528.2 eV), respectively, which indicates the existence of Ni-O-Ni type of structures [26]. Fig. 3J shows that the N1s spectrum of Ni $(OH)_2$-glycerate@CN can be interpreted into three characteristic peaks located at 397.7, 399.4, and 402.7 eV, assigning to nitrogen species (pyridinic, pyridonic and pyrrolic, nitrogen oxides) with the content of 22.6, 69.8, and 7.6%, respectively [27]. Interestingly, the N1s spectrum (Fig. 3K) acquired for Ni/NiO @NPGC exhibits N peak (pyridonic and pyrrolic nitrogen) at 400.1 eV. The analysis results shows clearly that the area of N-pyridonic and N-pyrrolic peak considerably decreases (from 69.8 to 46.5%), pyridinic nitrogen peak (at 397.9 eV, peak area changes from 22.6 to 37.4%) and nitrogen oxides peak considerably increases (at 403.1 eV, peak area changes from 7.6 to 16.1%), demonstrating that N-pyridonic and N-pyrrolic are converted to pyridinic nitrogen. According to previous reports, the contribution of N-doped states to the electrochemical performance of Ni/NiO@NPGC can be explained as follows [28]. On the one hand, the graphitic N can generate more defects which offer additional electrons transport channels for active sites of the Ni/NiO@NPGC. On the other hand, the pyridinic N with the lone pair of electrons is electrochemically active, which can easily conjugate with the carbon π-rings [24].

The composition of materials were displayed by XRD analysis (Fig. 3L and Fig. 3M). The $Ni(OH)_2$ phases were verified in the $Ni(OH)_2$-glycerate and $Ni(OH)_2$-glycerate@CN [29]. The cubic NiO and metallic Ni phase with strong diffraction peaks were confirmed in the Ni/NiO@NPGC. It was consistent with the XPS and HRTEM results. The Raman spectra of Ni/NiO@NPGC is shown in Fig. 3N where two peaks at 1340 and 1580 cm^{-1} correspond to the D and G bands of carbon [30]. In the Ni/NiO@NPGC, the intensity ratio (I_D/I_G) value is 1.08, implying the carbon composite was highly graphitized.

Moreover, the porous structure on the Ni/NiO@NPGC ball is confirmed by nitrogen adsorption–desorption isotherm and pore size distribution (Fig. 3O). The BET surface area of Ni/NiO@NPGC is calculated as 229.41 $m^2\ g^{-1}$, much larger than that of capsule-like NiO nanoparticles (48.9 $m^2\ g^{-1}$) [31] and Porous NiO Film (95 $m^2\ g^{-1}$) [32]. It was seen from the inset that its pore size is about 50 nm.

The Ni/NiO@NPGC with distinct pomegranate-like structure supply some advantages: 1) the metal oxides can be separated enough to prevent from self-agglomeration but keep the mass transfer paths at the same time, which further help to preserve the electrocatalytic activities; 2) the carbon frame of the structure serves as electron tunnels and connecting backbones, which ensure the electrochemical activities of all nanoparticles; 3) the active sites for electrochemical processes are located at Ni/NiO nanocrystals seeds with low dimension and large surface area; 4) the better environment to load enzymes can be achieved due to the Nitrogen-doped, partially graphitized carbon layer, which not only offers enhanced conductivity, chemical stability, and increased electrocatalytic activity, but also extended surface area as well as decent amount of mesoporous area [28]. The above advantages of as-prepared material are beneficial to the immobilization of the enzyme and methanol oxidation.

3.2. *Electrochemical behaviors of AChE modified electrodes and methyl parathion determination.*

The constituents of the biosensor (the amount of NF-NiO/Ni@ NPGC and enzyme) and the test conditions (pH and inhibition time) play a crucial role in realizing good analytical performance (See Fig.S-2 in Supporting Information). As a result, 0.216 U of AChE, 6 μL of NF-NiO/Ni@NPGC, a pH 7.5 of PBS, and 12 mins of the incubation time were chosen as subsequent experiment conditions.

3.2.1. *Electrochemical behaviors of AChE modified electrodes.*

As shown in the Nyquist plots (Fig. 4A), the charge transfer resistance (R_{et}) of Ni/NiO@NPGC/CPE is much smaller than NF/Ni/NiO@NPGC/CPE, NF/AChE /NF/Ni/NiO@NPGC/CPE and bare CPE, suggesting the high electric conductivity of Ni/NiO@NPGC. When the AChE was immobilized on the surface of NF/Ni/NiO@NPGC/CPE, it was observed that the R_{et} increased obviously. This phenomenon is attributed to the dielectric behavior of AChE enzyme molecules.

Fig. 4B represents the DPVs of different modified electrodes in PBS. No signal was observed at different modified electrodes for the lack of ATCl. After 1.5 mM ATCl was added into the PBS, there is a prominent oxidation peak at NF/AChE/NF-Ni/ NiO@NPGC/CPE. The electrochemical response comes from the oxidation of thiocholine (TCh). The pomegranate-like ball structure consists of porous 'pomegranate shell' and the good conductivity of 'pomegranate seeds', which not only provide more space to increase AChE immobilization amount, but also facilitate the accessibility of electron transfer. The influence of the scan rate on the CV performance of AChE electrode was explored in 1.5 mM ATCl. As can be seen from Fig. S-3, the anodic peaks intensity linearly increased with increasing scan rate from 0.02 to 0.3 $V{\cdot}s^{-1}$, which means this is a surface-controlled process.

3.2.2. *Methyl parathion (MP) determination.*

The DPV curves of NF/AChE/NF-NiO/Ni@NPGC/CPE biosensor upon additions of MP are shown in Fig. 4C. When add the MP in the incubation continually, the electrochemical response decreased gradually. From Fig. 4D, the linear range was found to be $1.0 \times 10^{-14} \sim 1.0 \times 10^{-8}$ $g{\cdot}mL^{-1}$ with the limit of detection (LOD) 3.5×10^{-15} $g{\cdot}mL^{-1}$ (1.2×10^{-14} M) for MP. Compared with other AChE biosensors listed in Table 1, the present NF/AChE/NF-NiO/Ni@ NPGC/CPE biosensor could be used in the detection of MP at low concentration.

The manufactures reproducibility for the effective biosensor was accomplished by comparing their electrochemical response for ATCl. The RSDs obtained were 4.8 % (n = 6), which means that a superior reproducibility of the biosensor. After being stored at 4 °C in the refrigerator for 4 weeks, the electrodes retained 96 %, 94 %, 91 % and

86 % of its initial peak current response in PBS containing 1.5 mM ATCl (Fig. 4E), indicating the good long-term stability for the biosensor.

Through comparing the NF/AChE/NF-NiO/Ni@NPGC/CPE electrochemical response for ATCl and other potential interfering compounds, the selectivity of the biosensor was investigated in PBS. There was no noteworthy influence on the detection of 0.5 mM ATCl in the presence of 0.5 mM glucose, $H_2C_2O_4$, citric acid, SO_4^{2-}, NO_3^- (Fig. 4F). The results indicated the biosensor displayed good selectivity.

3.2.3. Applications in real samples

To demonstrate the applicability of the biosensor in real samples, the analysis of apple and Chinese cabbage samples bought from a local market was carried out, whose measurement processes are shown in the Supporting Information S5. As shown in Table S1 in Supporting Information, the recoveries of MP in the supernatant of real sample diluted with PBS were in the range of 91.0%-96.7%. The RSD values were less than 5%, indicating that NF/AChE/NF-NiO/ Ni@NPGC/CPE biosensor displayed good analytical performance.

3.3. Electrocatalytic oxidation of Ni/NiO@NPGC modified electrodes for methanol.

3.3.1. Surface activation.

Fig. 5A compares CVs of the different modified electrodes for MOR in 1.0 M KOH solution containing 0.5 M methanol at 50 $mV{\cdot}s^{-1}$. It's easy to see the raising of oxidation current density for the $Ni(OH)_2$-glycerate@CN and $Ni(OH)_2$-glycerate electrodes. In sharp contrast, the NF-Ni/NiO@NPGC/GCE electrode demonstrated a remarkably enhanced anodic peak at + 0.63 V (vs. Hg/HgO). Obviously, the NF-Ni/NiO@NPGC/GCE exhibited a significantly electrocatalytic activity, signifying that the pomegranate-like structure together with the Ni/NiO@NPGC can intensively strengthen the electrochemical activity of the Ni/NiO@NPGC catalyst for MOR. The unique pomegranate-like composite architecture can provide a larger electrochemical active area, which was evaluated from electrochemical double-layer capacitance (C_{dl}). The C_{dl} of 1.25 $mF{\cdot}cm^{-2}$ was obtained for NiO/Ni@NPGC. (Supporting Information, Fig. S-4). The impact of the scan rate (v) on the response of the Ni/NiO@NPGC/GCE was investigated in Fig. 5B and 5C. The oxidation peak currents increased with the increase of v from 0.03 to 0.2 $V{\cdot}s^{-1}$.

3.3.2. Influence of the methanol concentration.

Fig. 5D displays the CVs of the NF-Ni/NiO@NPGC/GCE in different methanol concentration. With increasing the methanol concentration, the oxidation peak of methanol shifts towards higher values, indicating that the oxidation intermediates which require higher potential cannot be completely oxidized in the anodic scan. In addition, Fig. 5E described the proportional relationship between the anodic peak current and the methanol concentration, proving that the diffusion of methanol is rate-determining step of reaction.

3.3.3. Electrode stability.

Fig. 5F compares the chronoamperograms obtained from the different electrode materials. In the early stage of catalytic reaction, the intermediate species such as CO, CHx, and CH_3O may poison the active site of the catalyst, which is the reason for the decrease of current density. Furthermore, it is obvious that the attenuation of the current for the NF-Ni/NiO@NPGC/GCE was relatively slower than that for the Ni$(OH)_2$-glycerate@CN and $Ni(OH)_2$-glycerate electrodes, implying that the NF-Ni/NiO@NPGC possesses a higher stability toward MOR.

The electro-oxidation mechanism of methanol over NiO was shown in Fig. 5G. Under alkaline conditions, NiO and $Ni(OH)_2$ were oxidized to NiOOH, which catalyzed the oxidation of methanol to produce formic acid. The electrocatalytic activity of NiOOH toward methanol was considered to arise from the unpaired d-electrons or empty orbitals associated, which are available for bond formation with absorbed species [15]. For Ni/NiO@NPGC, the pomegranate-like architecture structure with pyridinic N and its carbon frame served as electron tunnels and connecting backbones, which ensured the electrochemical activities of all nanoparticles. In addition, the metal oxides were dispersed enough to prevent from self-agglomeration and keep the mass transfer paths at the same time, which was also conducive to the improvement of the catalytic activity.

4. Conclusion

The efficient electrochemistry platforms based on Ni/NiO@NPGC were constructed. The proposed biosensor demonstrated a wide linear range of 1.0×10^{-14}-1.0×10^{-8} g mL^{-1} with the detection limit of 3.5×10^{-15} g mL-1 for MP determination. Meantime, Ni/NiO@NPGC exhibited high electrocatalytic activity and durability for MOR. The above results were mainly attributed to the pomegranate-like architecture structure with pyridinic N and carbon frame of Ni/NiO@NPGC, which ensured the electrochemical activities of all nanoparticles and immobilization of enzyme. In addition, the metal oxide was well dispersed to prevent from self-agglomeration and kept mass transfer paths. The work has a significant in crafting inexpensive and highly efficient electrode materials for electrochemical biosensors and MOR.

Declaration of Competing Interest

The authors declare that they have no known competing financial interests or personal relationships that could have appeared to influence the work reported in this paper.

Acknowledgments

The authors appreciate the support from the National Natural Science Foundation of China (No. 21575111) and the Scientific and Technological Research and Development Projects in Shaanxi Province (No. 2020GY-306).

Appendix A. Supplementary material

Supplementary data to this article can be found online at https://doi.org/10.1016/j.bioelechem.2022.108094.

References

[1] T.T. Tian, M.X. Liu, L.X. Chen, F.J. Zhang, X. Yao, H. Zhao, X.J. Li, D-amino acid electrochemical biosensor based on D-amino acid oxidase: Mechanism and high performance against enantiomer interference, Biosens. Bioelectron. 151 (2020), 111971, https://doi.org/10.1016/j.bios.2019.111971.

[2] K.D. Wang, C. Wu, F. Wang, M.H. Liao, G.Q. Jiang, Bimetallic nanoparticles decorated hollow nanoporous carbon framework as nanozyme biosensor for highly sensitive electrochemical sensing of uric acid, Biosens. Bioelectron. 150 (2020), 111869, https://doi.org/10.1016/j.bios.2019.111869.

[3] R. Gupta, N. Raza, S.K. Bhardwaj, K. Vikrant, K.H. Kim, N. Bhardwaj, Advances in nanomaterial-based electrochemical biosensors for the detection of microbial toxins, pathogenic bacteria in food matrices, J. Hazard. Mater. 401 (2020), 123379, https://doi.org/10.1016/j.jhazmat.2020.123379.

[4] P. Das, M. Das, S.R. Chinnadayyala, I.M. Singha, P. Goswami, Recent advances on developing 3rd generation enzyme electrode for biosensor applications, Biosens. Bioelectron. 79 (2016) 386–397, https://doi.org/10.1016/j.bios.2015.12. 055.

[5] G. Lu, F. Ning, J. Wei, Y. Li, C. Bai, Y. Shen, Y. Li, X. Zhou, All-solid-state passive direct methanol fuel cells with great orientation stability and high energy density based on solid methanol fuels, J. Power Sources 450 (2020) 227669.

[6] I. Martinaiou, A.H.A. Monteverde Videla, N. Weidler, M. Kübler, W.D.Z. Wallace, S. Paul, S. Wagner, A. Shahraei, R.W. Stark, S. Specchia, U.I. Kramm, Activity and degradation study of an Fe-NC catalyst for ORR in Direct Methanol Fuel Cell (DMFC), Appl. Catal. B-Environ. 262 (2020) 118217.

[7] G. Zhang, Z. Yang, W. Zhang, Y. Wang, Nanosized Mo-doped CeO_2 enhances the electrocatalytic properties of the Pt anode catalyst in direct methanol fuel cells, J. Mater. Chem. A 5 (2017) 1481–1487, https://doi.org/10.1039/c6ta09043e.

[8] G. Ren, Z. Zhang, Y. Liu, Y. Liang, X. Zhang, S. Wu, J. Shen, Facile Synthesis Of Composition-Controllable PtPdAuTe Nanowires As Superior Electrocatalysts For Direct Methanol Fuel Cells, Chem. Asian J. 15 (1) (2020) 98–105.

[9] Y. Yang, Q. Yan, Q. Liu, Y. Li, H. Liu, P. Wang, L. Chen, D. Zhang, Y. Li, Y. Dong, An ultrasensitive sandwich-type electrochemical immunosensor based on the signal

amplification strategy of echinoidea-shaped Au@Ag-Cu_2O nanoparticles for prostate specific antigen detection, Biosens. Bioelectron. 99 (2018) 450–457.
[10] M.-X. Chen, M. Zhu, M. Zuo, S.-Q. Chu, J. Zhang, Y. Wu, H.-W. Liang, X. Feng, Identification of catalytic sites for oxygen reduction in metal/nitrogen-doped carbons with encapsulated metal nanoparticles, Angew. Chem. Int. Edit. 59 (4) (2020) 1627–1633.
[11] M. Haskul, A.T. Ülgen, A. Döner, Fabrication and characterization of Ni modified TiO_2 electrode as anode material for direct methanol fuel cell, Int. J. Hydrogen Energ. 45 (2020) 4860–4874, https://doi.org/10.1016/j.ijhydene.2019. 12.060.
[12] J. Xie, C. Lei, W. Chen, Q. Xie, Q. Guo, B. Huang, Catalytic properties of transition metals modified nanoscale zero-valent iron for simultaneous removal of 4-chlorophenol and Cr (VI): Efficacy, descriptor and reductive mechanisms, J. Hazard Mater. 403 (2020), 123827, https://doi.org/10.1016/j.jhazmat.2020. 123827.
[13] M. Tyagi, M. Tomar, V. Gupta, Glad assisted synthesis of NiO nanorods for realization of enzymatic reagentless urea biosensor, Biosens. Bioelectron. 52 (2014) 196–201, https://doi.org/10.1016/j.bios.2013.08.020.
[14] X. Cui, P. Xiao, J. Wang, M. Zhou, W. Guo, Y. Yang, Y. He, Z. Wang, Y. Yang, Y. Zhang, Z. Lin, Highly Branched Metal Alloy Networks with Superior Activities for the Methanol Oxidation Reaction, Angew. Chem. 129 (16) (2017) 4559–4564.
[15] M. Song, Y. Song, W. Sha, B. Xu, J. Guo, Y. Wu, Recent Advances in Non-Precious Transition Metal/Nitrogen-doped Carbon for Oxygen Reduction Electrocatalysts in PEMFCs, Catalysts 10 (2020) 141, https://doi.org/10.1016/j.mcat.2020.110834.
[16] H. Robatjazi, H. Zhao, D.F. Swearer, N.J. Hogan, L. Zhou, A. Alabastri, M. J. McClain, P. Nordlander, N.J. Halas, Plasmon-induced selective carbon dioxide conversion on earth-abundant aluminum-cuprous oxide antenna-reactor nanoparticles, Nat. Commun. 8 (1) (2017), https://doi.org/10.1038/s41467-017-00055-z.
[17] K.N. Dinh, V.G. Gomes, Hybrid Ni/NiO composite with N-doped activated carbon from waste cauliflower leaves: A sustainable bifunctional electrocatalyst for efficient water splitting, Carbon 157 (2020) 515–524, https://doi.org/10.1016/j.carbon.2019.09.080.
[18] Y. Liang, Y. Li, H. Wang, J. Zhou, J. Wang, T. Regier, H. Dai, Co_3O_4 nanocrystals on graphene as a synergistic catalyst for oxygen reduction reaction, Nat. Mater. 10 (2011) 780–786, https://doi.org/10.1038/nmat3087.
[19] J. Masa, W. Xia, M. Muhler, W. Schuhmann, On the role of metals in nitrogen-doped carbon electrocatalysts for oxygen reduction, Angew. Chem. Int. Edit. 54 (2015) 10102–10120, https://doi.org/10.1002/anie.201500569.
[20] X. Xia, J. Tu, Y. Zhang, X. Wang, C. Gu, X.-B. Zhao, H.J. Fan, High-Quality Metal Oxide Core/Shell Nanowire Arrays on Conductive Substrates for Electrochemical Energy Storage, ACS Nano 6 (6) (2012) 5531–5538.
[21] J. Yan, W. Sun, T. Wei, Q. Zhang, Z. Fan, F. Wei, Fabrication and electrochemical performances of hierarchical porous $Ni(OH)_2$ nanoflakes anchored on graphene sheets, J. Mater. Chem. 22 (23) (2012) 11494.
[22] Y. Liu, N. Fu, G. Zhang, W. Lu, L. Zhou, H. Huang, Ni@NiO core/shell dendrites for ultra-long cycle life electrochemical energy storage, J. Mater. Chem. A 4 (2016) 15049–15056, https://doi.org/10.1039/c6ta05508g.
[23] J. Zhou, J. Lian, L. Hou, J. Zhang, H. Gou, M. Xia, F. Gao, Ultrahigh volumetric capacitance and cyclic stability of fluorine and nitrogen co-doped carbon microspheres, Nat. Commun. 6 (2015) 8503, https://doi.org/10.1038/ncomms9503.
[24] J. Lin, J. He, Y. Chen, Q. Li, B. Yu, C. Xu, W. Zhang, Pomegranate-like silicon/nitrogen-doped graphene microspheres as superior-capacity anode for lithium-ion batteries, Electrochim. Acta 215 (2016) 667-673, https://doi.org/ 10.1016/j.electacta.2016.08.147.
[25] S. Xu, X. Li, Z. Yang, T. Wang, W. Jiang, C. Yang, S. Wang, N. Hu, H. Wei, Y. Zhang, Nanofoaming to boost the electrochemical performance of $Ni@Ni(OH)_2$ nanowires for ultrahigh volumetric supercapacitors, ACS Appl. Mater. Inter. 8 (41) (2016) 27868–27876.
[26] S. Chu, K. Gerasopoulos, R. Ghodssi, Tobacco mosaic virus-templated hierarchical Ni/NiO with high electrochemical charge storage performances. Electrochim Acta 220 (2016) 184-192, https://doi.org/https://doi.org/10.1016/ j.electacta.2016.10.106.
[27] C. Ma, X. Shao, D. Cao, Nitrogen-doped graphene nanosheets as anode materials for lithium ion batteries: a first-principles study, J. Mater. Chem. 22 (2012) 8911–8915, https://doi.org/10.1039/c2jm00166g.
[28] B. Kumar, M. Asadi, D. Pisasale, S. Sinha-Ray, B.A. Rosen, R. Haasch, A. Salehi-Khojin, Renewable and metal-free carbon nanofibre catalysts for carbon dioxide reduction, Nat. Commun. 4 (2013) 1–8, https://doi.org/10.1038/ncomms3819.
[29] J. Yan, Z. Fan, W. Sun, G. Ning, T. Wei, Q. Zhang, R. Zhang, L. Zhi, F. Wei, Advanced Asymmetric Supercapacitors Based on $Ni(OH)_2$/Graphene and Porous Graphene Electrodes with High Energy Density, Adv. Funct. Mater. 22 (12) (2012) 2632–2641.
[30] J. Chang, X. Huang, G. Zhou, S. Cui, P. B. Hallac, J. Jiang, J. Chen, Multilayered Si nanoparticle/reduced graphene oxide hybrid as a high-performance lithium-ion battery anode, Adv. Mater. 26 (2014) 758-764, https://doi.org/https://doi.org/10.1002/adma.201302757.
[31] H.M. Shiri, M. Aghazadeh, Synthesis, characterization and electrochemical properties of capsule-like NiO nanoparticles, J. Electrochem. Soc. 159 (2012) 132–138, https://doi.org/10.1149/2.106206jes.
[32] L. Wang, G. Zhang, Y. Liu, W. Li, W. Lu, H. Huang, Facile synthesis of a mechanically robust and highly porous NiO film with excellent electrocatalytic activity towards methanol oxidation, Nanoscale 8 (2016) 11256–11263, https://doi.org/10.1039/c6nr01991a.
[33] J. Gong, Z. Guan, D. Song, Biosensor based on acetylcholinesterase immobilized onto layered double hydroxides for flow injection/amperometric detection of organophosphate pesticides, Biosens. Bioelectron. 39 (2013) 320–323, https://doi.org/10.1016/j.bios.2012.07.026.
[34] M. Wei, G. Zeng, Q. Lu, Determination of organophosphate pesticides using an acetylcholinesterase-based biosensor based on a boron-doped diamond electrode modified with gold nanoparticles and carbon spheres, Microchim. Acta 181 (2014) 121–127, https://doi.org/10.1007/s00604-013-1078-4.
[35] L. Peng, S. Dong, W. Wei, X. Yuan, T. Huang, Synthesis of reticulated hollow spheres structure $NiCo_2S_4$ and its application in organophosphate pesticides biosensor, Biosens. Bioelectron. 92 (2017) 563–569, https://doi.org/10.1016/j.bios.2016.10.059.